

1 DOI: <https://doi.org/10.1016/j.jeurceramsoc.2022.05.075>

2

3 **Additive manufacturing of lead-free KNN by binder jetting**

4

5 Marco Mariani^a, Ruben Beltrami^a, Emanuele Migliori^a, Laura Cangini^b, Elisa Mercadelli^{b*},
6 Carlo Baldisserrri^b, Carmen Galassi^{a,b}, Nora Lecis^a

7

8 ^a Department of Mechanical Engineering, Politecnico di Milano, Milano 20156, Italy

9 ^b CNR-ISTEC, Istituto di Scienza e Tecnologia dei Materiali Ceramici, Faenza 48018, Italy

10

11 *Corresponding author: elisa.mercadelli@istec.cnr.it

12

13 **Abstract**

14 Additive manufacturing of lead-free piezoceramics is of great interest, given the large request
15 of application-oriented designs with optimal performances and reduced material
16 consumption. Binder Jetting (BJ) is an additive manufacturing technique potentially suited
17 to the production of ceramic components, however the number of feasibility studies on BJ of
18 piezoceramics is extremely limited and totally lacking in the case of sodium-potassium
19 niobate (KNN).

20 In this work, as-synthesised powders are employed in the BJ 3D printing process.
21 Microstructural properties, such as porosity, grain size distributions, and phase composition
22 are studied by SEM, XRD and MIP (Mercury Intrusion Porosimetry) and compared to die-
23 pressed pellets. Analyses reveal considerable residual porosity (~40%) regardless of the
24 printing parameters, with a weak preferential orientation parallel to the printing plane. The
25 piezoelectric characterization demonstrates an outstanding d_{33} value of 80-90 pC N⁻¹. Finally,

26 Figures of Merits for the employment as porous piezoceramics in the direct mode are
27 presented.

28

29 **Keywords:** Binder jetting; Additive Manufacturing; Piezoceramic; Binder saturation;
30 Porosity.

31

32 **1. Introduction**

33 In the last decade, additive manufacturing (AM) has been increasingly adopted due to some
34 of its features, such as design freedom and speed of production, which give a competitive
35 advantage over conventional manufacturing. However, the commercialisation of such
36 processes and products has regarded mainly metallic items obtained by direct AM processes
37 (e.g., Laser- and Electron Beam- Powder Bed Fusion (L-PBF and EB-PBF), Direct Energy
38 Deposition (DED)), whereas ceramic materials are still facing considerable issues that have
39 left their shaping by additive manufacturing techniques at a preliminary stage [1,2].
40 Nonetheless, AM would find great opportunities for application in this class of material, in
41 particular when functional ceramics are considered, since they usually have to satisfy less
42 stringent mechanical requirements compared to metals or structural ceramics and could
43 benefit greatly from customised solutions [3]. In this scenario, indirect AM techniques such
44 as Fused Deposition Modelling (FDM), Stereolithography (SLA), and Binder Jetting (BJ),
45 are gathering attention because they allow achieving the shaping of components without the
46 need of high temperatures, and to reach high densification by sintering with treatments and
47 equipment like those employed by the press-and-sinter route.

48 Piezoceramics are employed widely in industries as electronics, healthcare, power
49 generation. In these cases, AM would allow achieving improved performances and reduce
50 material waste. Moreover, the possibility to design and manufacture complex structures and
51 novel architectures in a wide size-range scale, would pave the way towards new studies and

52 application fields such as integrated electronics, tissue engineering and other advanced
53 intelligent devices [4]. However, issues as sensitivity to processing conditions and absence
54 of raw materials tailored for this type of techniques have so far prevented their development
55 [5]. In addition, the EU ban on the use of lead-zirconate titanate (PZT) has further limited the
56 availability of resources that could fit these processes and grant acceptable performance [6].
57 So far, most studies have focused on the use of barium titanate BaTiO_3 (BT) for SLA. Either
58 BT or SLA have features that limit the field of potential applications. BT is a soft
59 piezoceramic, which makes it ideal for sensors but unstable at high temperature or when
60 subject to high mechanical loads and high voltages. On the other hand, SLA offers good
61 resolution and fast prototyping. However, the preparation of stable suspensions with
62 photosensitive polymers can be challenging, and there can be significant waste of feedstock
63 material at the end of the process. In this work, lead-free sodium-potassium niobate
64 $(\text{K}_{0.5}\text{Na}_{0.5})\text{NbO}_3$ (KNN) was singled out as the material of choice due to its hard
65 piezoelectricity, which makes it ideal for energy conversion applications, and BJ was
66 explored as a possible alternative route for its cold consolidation. To the authors' knowledge,
67 there is no previous literature on this combination of material and process. KNN has been
68 previously produced by SLA [7] and BJ has been employed by Sufiiarov et al., Chavez et al.,
69 and Gaytan et al. to manufacture BT [8–10].

70 Powders employed in binder jetting should typically have optimal flowability, determined by
71 both their (spherical) shape and proper particle size distribution (wide unimodal or bimodal),
72 to pack properly [11–13]. In our study, the powder was not optimised for additive
73 manufacturing use; however, it yielded optimal results when cold consolidated by die
74 pressing. Therefore, this study is aimed at assessing the feasibility of combining binder jetting
75 with ready-to-use powder to produce KNN components with comparable performance to that
76 of traditionally processed ones.

78 2. Materials and Methods

79 2.1. Materials

80 KNN powders were synthesised through a mechanochemical-activation-assisted solid-state
81 reaction method [14]. Na_2CO_3 (Merck, 99.5%), K_2CO_3 (Merck, 99%) and Nb_2O_5 (Aldrich,
82 99.99%) were dried at 80 °C for 24 h, weighed and planetary milled in a zirconia jar with a
83 Fritsch Planetary Mill (PULVERISETTE 6). Distilled water was used as dispersing medium
84 (2:1 water/powders weight ratio) while yttria-stabilized zirconia balls (2 mm diameter) were
85 used as milling media, setting 6:1 the balls-to-powder weight ratio. The milling was set to
86 last 100 min with a rotation speed of 600 rpm. The as-milled slurry was freeze-dried, and the
87 resulting powder sieved and calcined at 700 °C for 9 h. The as-calcined powder was
88 planetary-milled at 400 rpm for 120 min and finally freeze-dried and sieved. The as-obtained
89 powder was not subjected to any granulation processes before BJ.

90

91 2.2. Printing and Post-Processing

92 Small (diameter = 10 mm, thickness = 1 mm) and larger (diameter = 20 mm, thickness = 2
93 mm) disks were produced via BJ using an Innovent+ 3D printer by ExOne Inc. Prior to
94 printing, the powder was dried at 120 °C for 24 hours to remove residual humidity and obtain
95 a suitable flowability of the material through the hopper. The organic binder used for BJ was
96 the commercially available AquaFuse® (previously known as BA005), provided by ExOne
97 Inc.

98 Three different binder saturations (BS) were tested for the smaller geometries: 75%, 90% and
99 120%. **These values correspond to the ratio between the volume of the deposited binder and**
100 **that of the powder bed porosity.** All larger disks were, instead, printed at 90% binder
101 saturation. Layer thickness (LT) was kept constant at 50 μm to ensure good geometrical
102 resolution and minimise the risk of macropores formation, usually associated with the
103 spreading of larger layers with poorly flowing powders [15].

104 The powder bed was cured at 180 °C for 6 hours in air to obtain the polymerisation of the
 105 monomer dissolved in the binder and the evaporation of the residual solvents. The sintering
 106 process was performed in a sealed alumina crucible at 1130 °C for 2 hours with a 2.5 °C min⁻¹
 107 heating rate, in the presence of KNN pack powder with 2 wt.% alkali excess. The disks
 108 were densified by single and double sintering, where the latter consisted in densifying the
 109 samples through two consecutive sintering cycles separated by cooling of the specimens to
 110 room temperature.

111 Specimens obtained by different combinations of printing parameters, size, and sintering
 112 conditions are referred to as explained in Table 1.

113 Additionally, fully dense samples were produced by press-and-sinter to compare the
 114 properties of components obtained by additive and conventional manufacturing. These were
 115 densified for 2 hours at 1130 °C with a heating rate of 2.5 °C min⁻¹ in presence of pack
 116 powder, exactly as for the mono-sintered components.

117

118 **Table 1** Nomenclature of the specimens according to binder saturation (BS 75, 90, 120),
 119 the geometry size (S= small, L= large), and number of sintering cycles (1,2) performed.

Sample name	BS / %	Size	Number of sintering cycles
75S1	75	Small	1
90S1	90	Small	1
120S1	120	Small	1
90L2	90	Large	2

120

121 2.3. Characterisations

122 The KNN powder morphology was analysed by field emission-scanning electron
 123 microscopy (FE-SEM) in a ZEISS SIGMA 500 FE-SEM unit, while the particles size
 124 distribution was analysed by optical granulometry (ASTM E2651-19) using a Malvern

125 Morphology 4 unit (resolution = 150 nm), which allowed calculating the cumulative and
126 relative frequency curves of the number-based size distribution. An analysis of powder
127 flowability was obtained with a FT4 Powder Rheometer 2 that measured the values of
128 apparent density (ρ_{app}), corresponding to the as-poured material (ASTM B417-18), and
129 tapped density (ρ_{tap}) after compaction (ASTM B527-20). The Hausner (H) index, defined
130 as follows in Eq. 1, gave an estimate of the feedstock flowability:

$$131 \quad H = \rho_{tap} / \rho_{app} \quad (1)$$

132 X-ray diffraction (XRD) analyses on both the starting powder and the sintered samples were
133 performed over the $20^\circ \leq 2\theta \leq 80^\circ$ range (step size 0.02°) at a scanning rate of 1° min^{-1} with
134 Cu-K α radiation ($\lambda = 1.5406 \text{ \AA}$) in a Smartlab II Rigaku diffractometer. For XRD
135 measurements the sintered samples were prepared by grinding, sieving, annealing at 700°C
136 for 30 minutes, and an additional final sieving. The $\text{K}_{0.5}\text{Na}_{0.5}\text{NbO}_3$ phase was identified by
137 the structure file COD DB #2300499 [16]. Rietveld refinements of the diffraction patterns
138 were carried out using GSAS-II $\text{\textcircled{C}}$ (General Structure Analysis System) software.

139 The green and sintered densities of both small and large sized samples were evaluated by the
140 geometrical method. Relative density values were calculated with reference to the theoretical
141 density of 4.50 g cm^{-3} .

142 Both fracture surfaces and polished sections of the sintered samples were investigated by FE-
143 SEM. Grain size distribution of the ceramics was determined by machine learning
144 segmentation employing the trainable WEKA plugin of ImageJ on the SEM micrograph of
145 polished cross-section surface. The overall pore volume and the pore size distribution of the
146 sintered samples were calculated by Mercury Intrusion Porosimetry (MIP). The analysis was
147 performed in an Autopore V9600 unit built by the Micrometrics Instrument Corporation
148 (US). The Washburn equation (Eq. (1)) was employed to calculate the pore diameters from
149 the infiltration pressure at the different stages of the process:

150

151 $d = - (4 \gamma \cos\theta) / P$ (1)

152

153 where d is the diameter of the intruded pores, γ is the mercury surface tension (485.5 mN m⁻¹
154 at room temperature), θ is the contact angle between mercury and the surface of the pores
155 (for Hg-GDM the value recorded is 130°) and P is the external pressure applied to the
156 mercury by the instrument.

157 Silver-electroded samples were dielectrically, piezoelectrically and mechanically
158 characterised after the poling process (3 kV mm⁻¹ at 120 °C for 40 min), by acquiring their
159 room-temperature piezoresonance spectra with an HP 4194A (Hewlett Packard, US)
160 impedance analyser, detecting resonance and antiresonance frequencies over the 100 Hz–40
161 MHz range. Room-temperature capacitance and loss tangent were measured at 1 kHz using
162 the same instrument. Dielectric, piezoelectric, and mechanical parameters were calculated
163 according to the 1986 ASTM Standard on Piezoelectricity. d_{33} piezoelectric charge
164 coefficient values were separately measured using a Sinocera S 5865 d_{33} -meter calibrated
165 with a standard sample provided by the manufacturer. For the thicker 90L2 samples, the d_{33}
166 was calculated both along the parallel orientation and the perpendicular orientation with
167 respect to the layer deposition direction (Figure 1) to evaluate the possible effect of the
168 oriented porosity.

169 For clarity, _PAR and _PER are added to the samples name when necessary to distinguish
170 the properties measured in the parallel and perpendicular direction, respectively.

171



172

173 **Figure 1** Schematic representation of the d_{33} measurement direction with respect to the
 174 layer deposition orientation. Red areas represent the electrodes.

175

176 3. Results and Discussion

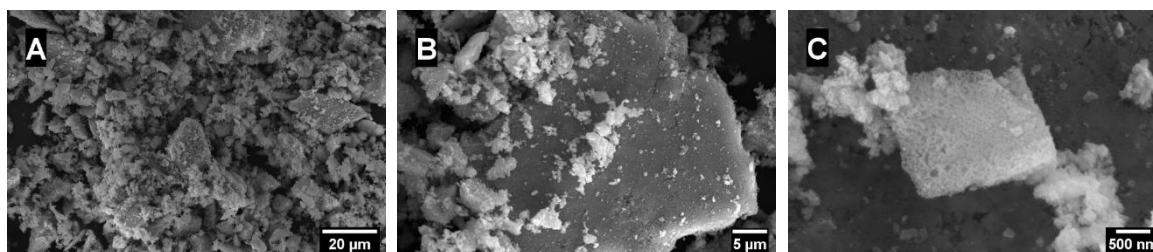
177 3.1 Morphological and microstructural characterization

178

179 3.1.1. KNN Powder

180 **The** SEM image in Figure 2A shows that powder particles have an irregular shape and their
 181 size covers an extended range. Indeed, ultra-fine sub-micron size particles were detected
 182 (Figure 2C); there are agglomerates whose dimension falls within the 1 to 10 μm range;
 183 finally, a few larger platelets-like fragments are also present. The finer fraction either **forms**
 184 irregular agglomerates or tends to stick to the flat surface of the larger particles (Figure 2B).

185



186

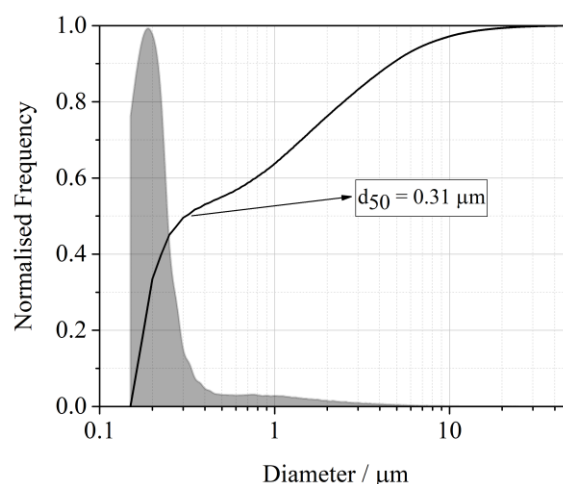
187 **Figure 2** SEM images of the KNN powder at different magnification levels.

188

189 **The results of the granulometric analysis** reported in Figure 3 confirmed the observations
 190 made by SEM analyses of particles size. As summarised in Table 2, most particles are in the

191 100 – 500 nm range, while agglomerates and platelets size is above 1.5 μm . It should be noted
192 that, during sample preparation for **the granulometric analysis**, particles dispersion occurs by
193 compressed air blowing, which may disaggregate some larger particles, thus increasing the
194 count of the finer fraction.

195 The wide particle size distribution may improve the packing of the powder, with smaller
196 granules filling the voids between the larger ones, and the fine fraction might be helpful in
197 promoting the sintering mechanisms during post-printing treatments [17–19]. However, it
198 should also be considered that small dimensions in combination with irregular shape could
199 severely impair the flowability of the material [20,21].



200

201 **Figure 3** Cumulative (solid line) and relative frequency (grey area) distribution curves of
202 KNN powder.

203

204 The Hausner ratio (H) is much higher than 1.2, the threshold value for a properly flowing
205 powder (Table 2) [22]. Factors influencing flowability are **the** low density of the powder, its
206 hygroscopicity, and its irregular shape, which favour the formation of low-density aggregates
207 due to electrostatic interactions, capillarity, and mechanical interlocking [22,23]. In this case,
208 the only improvement could be obtained by completely drying the powder before printing,
209 as described in Paragraph 2.2, to remove residual humidity.

210 In addition, the intrinsic porosity of the powder is particularly relevant, as shown by the
 211 extremely low relative density even after compaction, as evidenced by the tapped density
 212 values (Table 2).

213

214 **Table 2** Granulometric (particle size (μm) distribution values) and rheometric (apparent
 215 density (%), tapped density (%) and Hausner ratio) values obtained from measurements on
 216 KNN powder.

Granulometry			Rheometry		
$d_{10} / \mu\text{m}$	$d_{50} / \mu\text{m}$	$d_{90} / \mu\text{m}$	$\rho_{\text{app}}^{(I)} / \%$	$\rho_{\text{tap}}^{(I)} / \%$	H
0.15	0.31	4.69	13.8 ± 1.3	24.6 ± 1.5	1.78 ± 0.1

217 (I) expressed as a percentage of solid state KNN bulk density (4.50 g cm^{-3}).

218

219

220 3.1.2. Green Body

221 The printing procedure seems to be slightly beneficial to the packing of the powder. Indeed,
 222 all the printed samples featured a relative green density higher than 30% (32, 34, and 35%
 223 for 75S1, 90S1, and 120S1 KNN sample respectively), while the tapped density was only
 224 $24.6 \pm 1.5 \%$ (Table 2). This might be explained by two factors: first, the binder partially fills
 225 the voids of the powder bed (depending on binder saturation), thus contributing its own
 226 weight to that of the sample; second, the layer-by-layer deposition and the spreading action
 227 of the roller on a limited amount of material may favour the rearrangement of the particles,
 228 which could prevent excessive formation of voids in the powder bed [21,23]. The
 229 contribution from the binder weight seems to be confirmed by the correlation between binder
 230 saturation and green density.

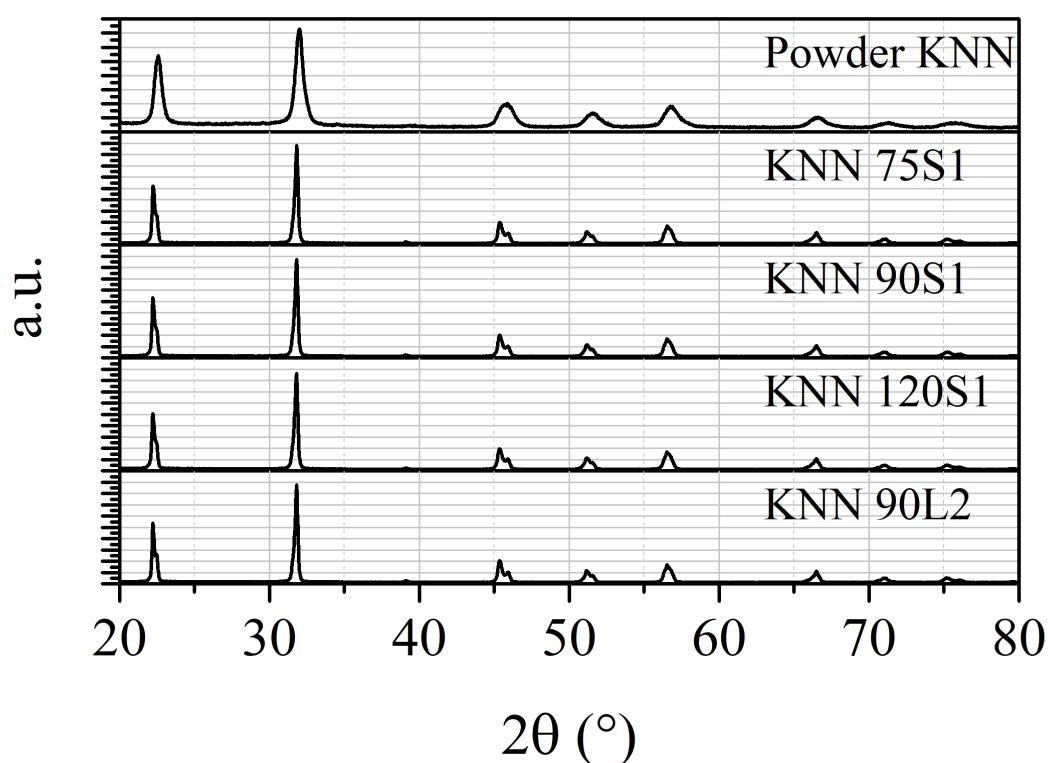
231

232 3.1.3. Sintered samples

233

234 XRD analyses were performed on mono-sintered and bi-sintered samples (Figure 4). The
235 XRD spectra are compared to the one registered for the KNN powder. The results highlight
236 that - both in powders and sintered samples - only $\text{K}_{0.5}\text{Nb}_{0.5}\text{O}_3$ peaks are present, and that
237 no secondary phases are formed during the selected thermal treatments
238 (calcination/sintering). In particular, the XRD spectra and the calculated unit-cell parameters
239 of the sintered samples (Table 3) demonstrate that neither structural changes nor secondary
240 phases occur using different binder saturations (75S1, 90S1, and 120S1) or after a second
241 sintering treatment (90L2). While, the broad peaks of the powder pattern once again
242 emphasize the role of the finer particles fraction [24].

243



244

245 **Figure 4** XRD spectra of the KNN powder, mono-sintered samples (75S1, 90S1, 120S1)

246

and bi-sintered sample (90L2).

247

248 **Table 3** Refinement agreement factors and unit-cell parameters for the sintered KNN
 249 samples.

Sample	Refin. agreement factors			K _{0.5} Na _{0.5} NbO ₃ phase				
	R _w %	χ^2_r 	GOF 	R ² %	a	b Å	c	Cell volume Å ³
KNN 75S1	7.9	3.57	1.89	2.81	3.956	5.636	5.665	126.316
KNN 90S1	7.74	3.41	1.85	3.09	3.956	5.637	5.665	126.325
KNN 120S1	7.71	3.41	1.85	2.72	3.956	5.636	5.665	126.314
KNN 90L2	7.8	3.38	1.84	3.15	3.955	5.638	5.665	126.324

250

251

252

253 After a single sintering cycle, all samples feature a reduced shrinkage and significant
 254 differences are not observed between different binder saturations. However, it should be
 255 noted that the limited size and some distortion of the disk planar surface hindered the
 256 acquisition of very precise geometrical measurements. The density values obtained
 257 corresponded to 29.5 ± 0.5 %, 30.3 ± 0.4 %, and 31.8 ± 1.1 % for the 75S1, 90S1 and 120S1,
 258 respectively. These densities are slightly lower than those of the green samples, which is
 259 likely due to the saturation of the binder: at the green stage, the binder own weight gives a
 260 sizable contribution to that of the samples; however, during the sintering process, the polymer
 261 is completely pyrolyzed and removed, thus generating additional open porosity inside the
 262 microstructure that is not compensated for during sintering, which likely featured mainly
 263 surface diffusion mechanisms that did not promote densification [25,26]. In addition, an
 264 excessive amount of binder might lead to the risk of overfilling the voids, thus pushing the
 265 particles apart and increasing the distance among them [13,27].

266 SEM micrographs of cross-section surfaces in Figure 5 confirm the presence of significant
 267 internal porosity. It is possible to distinguish three types of voids in the microstructure:

- 268 • inter-layer cracks and fractures of varying length, up to 300 μm in some cases (Figure
 269 5A);

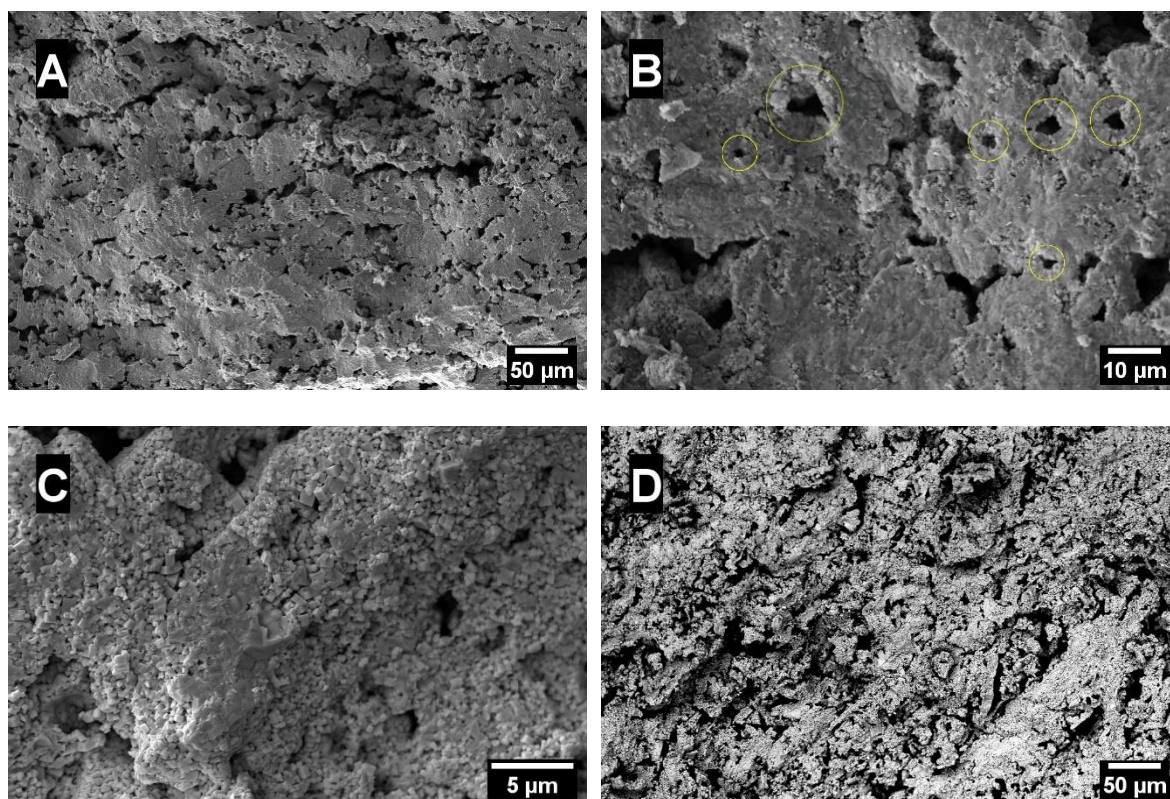
- 270 • macropores placed along the layer surfaces, likely formed in between the single binder
271 droplets during the printing phase (1 - 15 μm) (Figure 5B);
- 272 • micropores within the densified regions resulting from the incomplete closure of the
273 dihedral pores in between KNN grains (Figure 5C).

274 The porosity distribution in the sintered samples is confirmed by results of MIP performed
275 on the 90S1 sample, shown in Figure 6A. In addition, Figure 5A shows that the macroporosity
276 is preferentially oriented along the layer surface, which could result in an anisotropic
277 piezoelectric behaviour, particularly desired in porous piezoceramics working in the d_{33}
278 mode.

279 Figure 5D shows the cross-section fracture surface of the 120S1 sample. While the samples
280 75S1 and 90S1 show similar microstructures, this material is characterised by an even wider
281 network of macropores and large voids, which is likely the result of the excessive amount of
282 binder. During printing, this overfilling mechanism might generate a local pressure on the
283 powder bed and move the particles away from each other. After binder removal, this could
284 result in a decrease of the number of contact points, which hinders the formation of necks
285 and the diffusion mechanisms during sintering.

286 An important observation is that grain growth is quite limited: most grains have size below
287 1 μm , as can be seen from the frequency distributions in Figure 6B. Usually, **domination of**
288 **non-densifying mechanisms, being surface diffusion the most prevalent one, occurs at initial**
289 **stage of KNN sintering causing rapid grain growth and poor densification** [28,29]. In our
290 case, **however**, the material featured only initial stage sintering **without observation of**
291 **abnormal grain growth since the final** relative density is below **40%**. This is likely due to the
292 very small density of green bodies, which reduced the coordination number of the particles
293 and increased the activation energies of both surface and volume diffusion mechanisms.

294

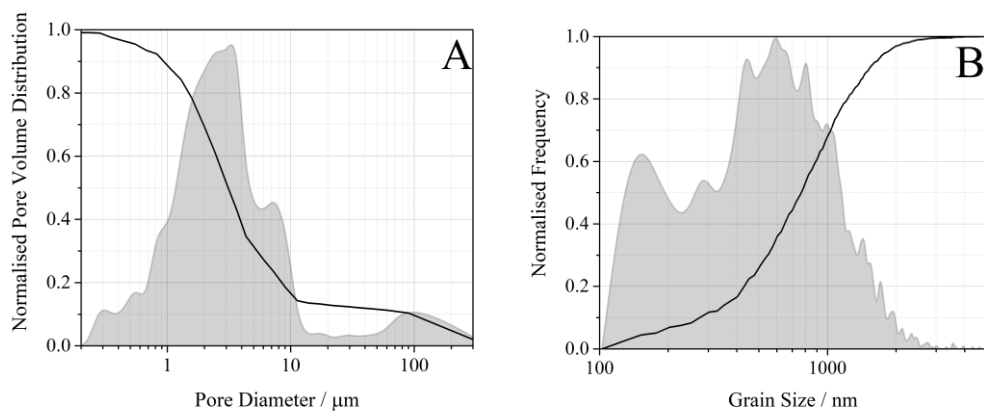


295

296

297 **Figure 5** SEM micrographs of (A-B) the fracture surface of 90S1 sample, (C) the fracture
 298 surface of 75S1 sample and (D) the fracture surface of 120S1 sample.

299



300

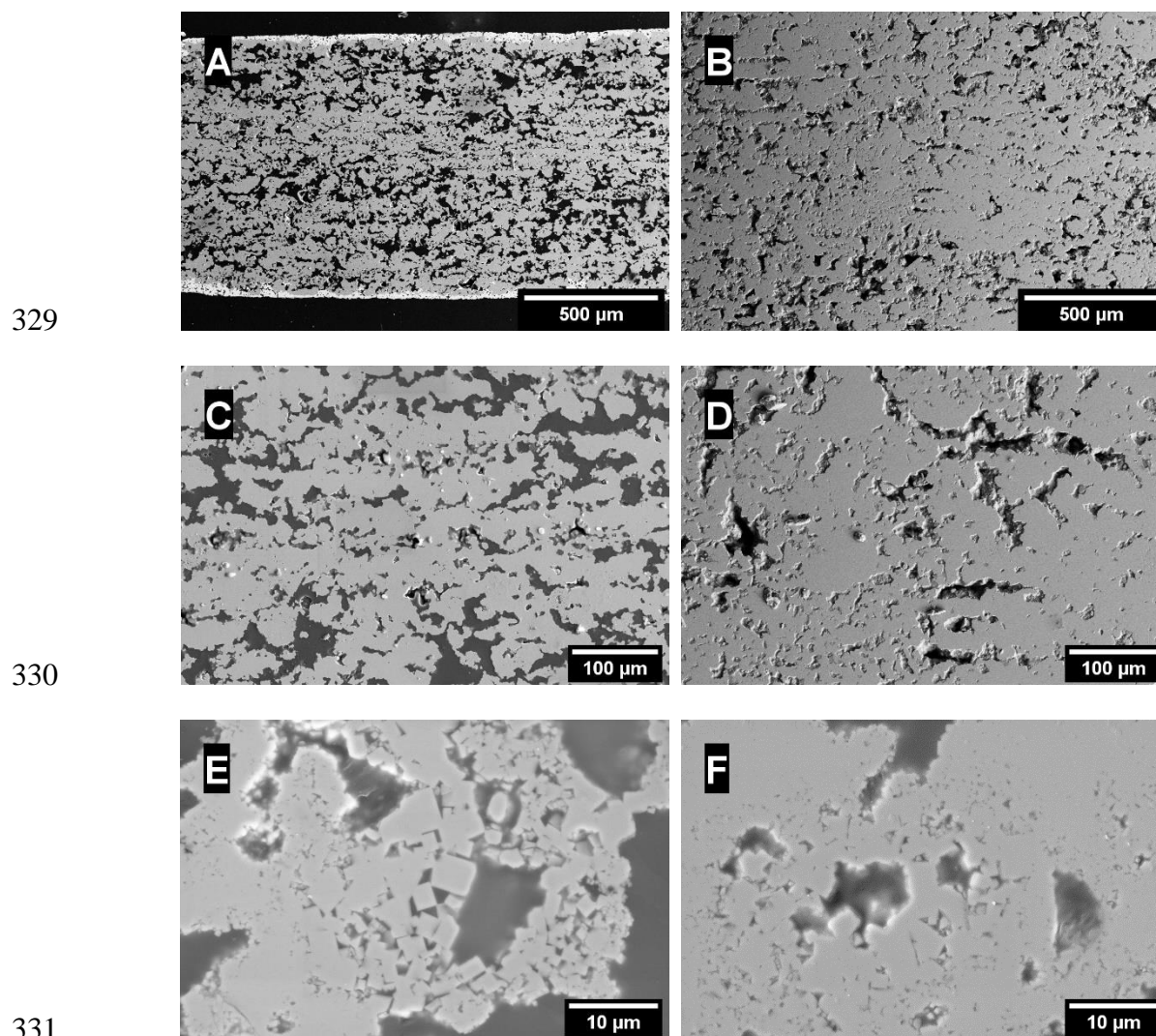
301 **Figure 6** Microstructural features size: (A) Cumulative (solid line) and relative (grey area)
 302 porosity volume distribution obtained by MIP measurements on sample 90S1; (B)
 303 Cumulative (solid line) and relative (grey area) distributions of the grains size of the 90S1
 304 sample.

305

306 To improve the final density of the KNN ceramics produced via BJ, a subsequent second
307 sintering treatment at 1130 °C for 2h was employed for the 90L2 sample. However, it appears
308 from the SEM images in Figures 7C and 7D that the additional thermal treatment promotes
309 only partially the sintering mechanisms to enhance the densification. A final relative density
310 of 56 % was in fact achieved after the second sintering step. This confirms again the poor
311 sinterability of KNN-based systems due to the domination of non-densifying material
312 transport mechanism, i.e. surface diffusion. The low activation energy of the latter induces
313 the grain growth during the heating step, reducing the driving force for sintering during the
314 main sintering stage [28].

315 It should also be noted that coarsening might be an issue, as larger grains tend to grow further
316 generating microporosities at their boundary (Figures 7E and 7F). Volume diffusion
317 mechanisms, that are responsible for large densification gradients, seem to not have occurred,
318 which is coherent with the low final density. SEM micrographs on polished cross and
319 longitudinal sections (Figure 7A and 7B) confirm that a well-oriented microstructure is
320 absent, in particular in those regions of the solid where porosity is more relevant. It could be
321 expected that an improvement of the final density could lead to a clearer distinction of the
322 interlayer porosity, as observed in other studies [30–32]. On the one hand, this result
323 highlights that exploiting BJ to achieve oriented microstructural development is more
324 challenging than with other techniques like freeze-casting, where directional sintering is
325 enhanced [33,34]. On the other hand, a more homogeneous internal structure allows a greater
326 freedom of design since optimal performance is granted independently from the orientation
327 considered.

328



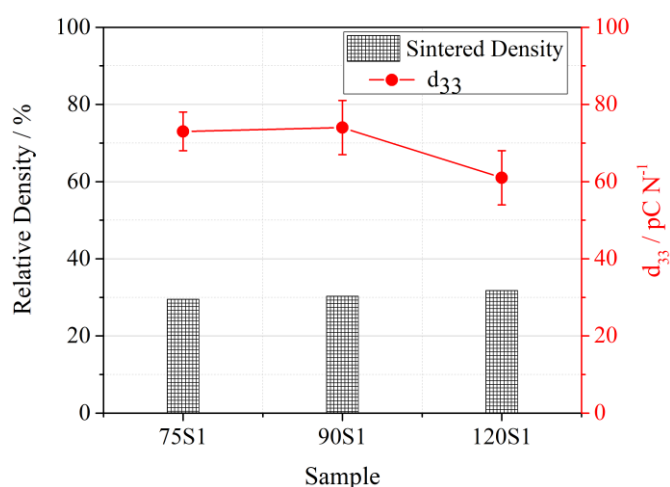
332 **Figure 7** SEM micrographs of **90L2** bi-sintered components, specifically: (A, C, and E)
 333 polished cross section (perpendicular to the layer orientation) at different magnifications;
 334 (B, D, and F) polished longitudinal section (parallel to the layer orientation) at different
 335 magnifications.

336

337 *3.2 Functional properties*

338 d_{33} values measured for the three mono-sintered samples are promising if correlated with the
 339 extent of their densification (Fig. 8), except for the 120S1 sample, the response of the latter
 340 being 10 pC N⁻¹ lower. Indeed, samples with higher density values (~ 92% relative density)
 341 obtained from the same powder by the pressing and sintering technique featured a d_{33} value
 342 of 105.6 ± 2.9 pC N⁻¹; the d_{33} value of the 90S1 sample is 70.5% with respect to that of the

343 92% relatively dense sample, which is larger than expected based on the ratio between the
 344 relative densities. 120S1 featured the lowest final d_{33} piezoelectric charge coefficient and the
 345 largest $\tan(\delta)$ values (61 pC N^{-1} and 70%, respectively). The lack of an electrical path
 346 continuity or excessive tortuosity of the same could hinder the material polarization under an
 347 electric field, thus being responsible for the lower piezoelectric response of this sample.
 348



349

350 **Figure 8** Sintered density and d_{33} values of the mono-sintered thin samples.

351

352 d_{33} measurements performed on the bi-sintered 90L2 sample (Table 4) show even higher
 353 piezoelectricity as compared to that of mono-sintered samples, with d_{33} values closer to those
 354 measured on dense samples. This could be attributed to the improved structural integrity of
 355 these samples compared to the thinner ones, likely due to the double sintering process and to
 356 the larger ratio between sample thickness and largest internal porosity or defects size (~ 100
 357 μm), which may be relevant in case of production of complex geometries where thickness
 358 variations may be responsible for varying piezoelectric performance in different regions of
 359 the component. The first hypothesis is confirmed by the higher values of relative density that
 360 were achieved after the second sintering step, as can be seen in Table 4.

361 On the other hand, the effect of porosity orientation seems to be minimal. Values in Table 4
 362 show a ~ 5 pC N⁻¹ improvement of the d_{33} measured parallel to the layers deposition
 363 orientation that can be attributed to better structural continuity in this direction that increases
 364 the mechanical stiffness of the ceramic [9,35]. However, many contact surfaces between
 365 sintered layers are present, which hinder the unambiguous detection of differences in the
 366 piezoelectric behaviours of the 90L2_PER and 90L2_PAR samples.

367

368 **Table 4** d_{33} values measured for the 90S1 (mono-sintered), 90L2_PER and 90L2_PAR (bi-
 369 sintered) samples.

	90S1	90L2_PAR	90L2_PER	DENSE
d_{33} / pC N ⁻¹	74.1 ± 7.0	84.8 ± 9.2	89.9 ± 3.8	105.6 ± 2.9
Q_m	22.3	27.4	-	72.7
Relative density / %	30.3 ± 0.4	55.6 ± 4.4		92.3

370

371 Although the printed samples are still very porous, and structural integrity needs to be
 372 improved, the piezoelectric properties of KNN bodies obtained by binder jetting are
 373 promising according to the Figures of Merit (FoM) typically required of porous
 374 piezoceramics. Usually, porous piezoceramics are employed in the direct mode and the
 375 related FoM₃₃ is calculated according to Eq. 2, as described in [36]:

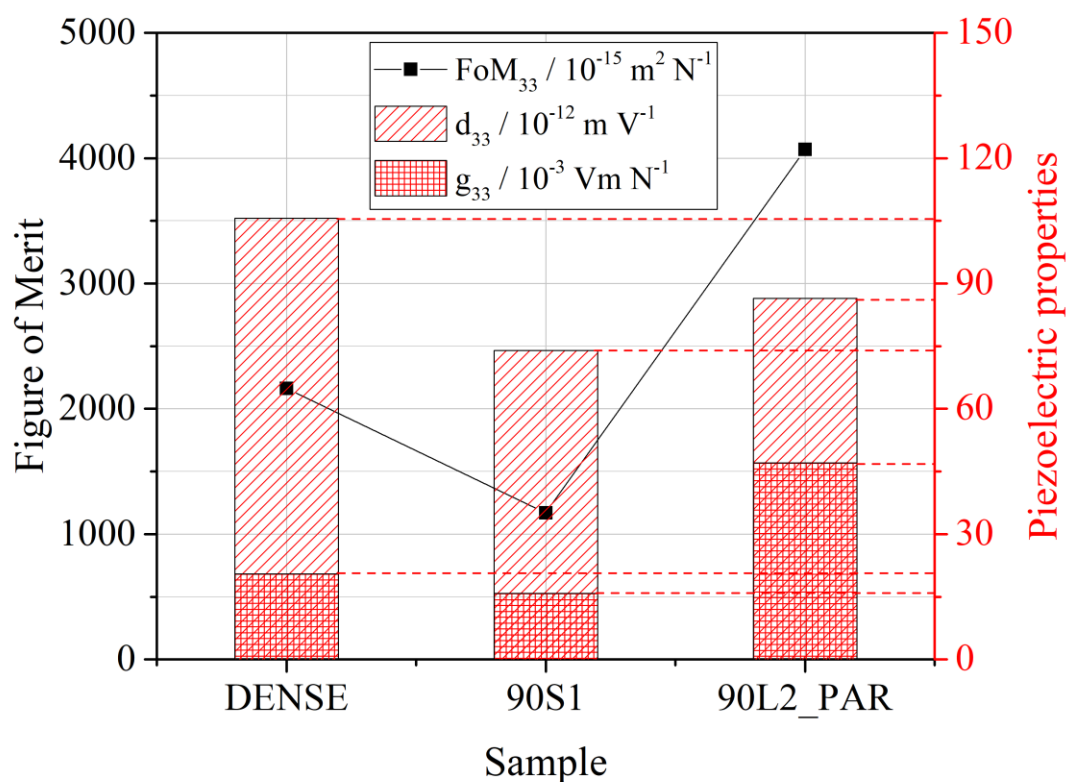
376

$$377 \text{FoM}_{33} = d_{33} g_{33} \quad (2)$$

378

379 It can be seen from the graph in Figure 9 that the printed samples subjected to the double
 380 sintering process feature an almost 100% improvement over the dense component obtained
 381 by traditional press-and-sinter technology. This is due to the proportionally larger increase
 382 of dielectric permittivity over d_{33} loss, as reported also by other studies [34,36,37].

383 Further investigation is needed to improve the mechanical and functional performances of
 384 these components, however it should be noted that the presented results already open the
 385 possibility of exploiting binder jetting for specific applications where porous piezoceramics
 386 may be advantageous over their dense counterpart [4,33,36,38].
 387



388

389 **Figure 9** Comparison of the piezoelectric performance of the dense and porous samples.

390

391 In Figure 10 an example of very small samples with complex geometry that can be produced
 392 by binder jetting is shown; the morphology of the starting powders must be further optimised
 393 in order to improve the accuracy and the surface finishing.

394



395

396 **Figure 10** Sintered KNN samples of complex geometry produced by binder jetting.

397

398

399

400

401 **4. Conclusions**

402 This study assesses the feasibility of producing KNN samples of complex geometry by binder
403 jetting starting from as-synthesised powder; it exemplifies the possibility to adopt this
404 additive manufacturing technique for the shaping of functional ceramics.

405 The powder packing behaviour and morphology of the green specimens demonstrate that
406 even though raw materials still feature a poor flowability, relative density values above
407 expectation may be achieved, thanks to the layer-by-layer deposition that reduces the risk of
408 macropores formation within the powder bed. In this case, average green density values
409 ranged in between ~30% and ~35%, depending on the binder saturation employed during
410 printing, with at least a +5% improvement over tap density measured from rheometry.

411 Nevertheless, such low green compaction values **limited the densification** of the samples and
412 the sintering cycle needed **to be repeated** to achieve larger than 50% sintered density and
413 sufficient mechanical integrity to allow safe handling of the specimens. Micrographs parallel

414 and perpendicular to the printing planes suggest slight porosity anisotropy, which weakly
415 affected the piezoelectric performances.

416 Finally, the increase of the Figure-of-Merit of the porous samples over the dense one paves
417 the way towards new applications of the binder jetting 3D printing technique in the area of
418 functional ceramics with complex shapes.

419

420

421 **Acknowledgements**

422 Authors would like to acknowledge the “Functional Sintered Materials (Funtasma)”
423 Interdepartmental Laboratory of Politecnico di Milano, where this research activity was
424 partially developed. Support by the Italian Ministry for Education, University and Research
425 through the project Department of Excellence LIS4.0 (Integrated Laboratory for Lightweight
426 e Smart Structures) is also acknowledged. EM and LC acknowledge the support from the
427 project “DIGIMAN – Soluzioni per la DIGItalizzazione delle aziende nel settore
428 MANifatturiero” – PG/2018/631166, in the frame of the POR FESR 2014-2020 programme
429 of the Regione Emilia Romagna (Italy).

430

431

432 **References**

- 433 [1] D. Huson, 3D printed ceramics: Current challenges and future potential, in: Int. Conf.
434 Digit. Print. Technol., 2016: pp. 374–377.
435 [https://doi.org/https://www.ingentaconnect.com/content/ist/nipdf/2016/00002016/00](https://doi.org/https://www.ingentaconnect.com/content/ist/nipdf/2016/00002016/0000001/art00094)
436 [000001/art00094](https://doi.org/https://www.ingentaconnect.com/content/ist/nipdf/2016/00002016/0000001/art00094).
- 437 [2] Y. Zhang, L.M. Wu, X.Y. Guo, S. Kane, Y.F. Deng, Y.G. Jung, J.H. Lee, J. Zhang,
438 Additive Manufacturing of Metallic Materials: A Review, J. Mater. Eng. Perform. 27

- 439 (2018) 1–13. <https://doi.org/10.1007/s11665-017-2747-y>.
- 440 [3] Y. Lakhdar, C. Tuck, J. Binner, A. Terry, R. Goodridge, Additive manufacturing of
441 advanced ceramic materials, *Prog. Mater. Sci.* 116 (2021) 100736.
442 <https://doi.org/10.1016/j.pmatsci.2020.100736>.
- 443 [4] E. Mercadelli, C. Galassi, How to Make Porous Piezoelectrics? Review on Processing
444 Strategies, *IEEE Trans. Ultrason. Ferroelectr. Freq. Control.* 68 (2021) 217–228.
445 <https://doi.org/10.1109/TUFFC.2020.3006248>.
- 446 [5] C. Chen, X. Wang, Y. Wang, D. Yang, F. Yao, W. Zhang, B. Wang, G.A. Sewvandi,
447 D. Yang, D. Hu, Additive Manufacturing of Piezoelectric Materials, *Adv. Funct.*
448 *Mater.* 30 (2020) 2005141. <https://doi.org/10.1002/adfm.202005141>.
- 449 [6] European Parliament, Directive 2011/65/EU of the European Parliament and of the
450 Council of 8 June 2011 on the restriction of the use of certain hazardous substances in
451 electrical and electronic equipment (RoHS), *Off. J. Eur. Union.* 54 (2011) 88–110.
452 [https://eur-lex.europa.eu/legal-content/EN/TXT/?uri=CELEX%3A02011L0065-](https://eur-lex.europa.eu/legal-content/EN/TXT/?uri=CELEX%3A02011L0065-20210401)
453 [20210401](https://eur-lex.europa.eu/legal-content/EN/TXT/?uri=CELEX%3A02011L0065-20210401) (accessed October 17, 2021).
- 454 [7] W. Chen, F. Wang, K. Yan, Y. Zhang, D. Wu, Micro-stereolithography of KNN-based
455 lead-free piezoceramics, *Ceram. Int.* 45 (2019) 4880–4885.
456 <https://doi.org/10.1016/j.ceramint.2018.11.185>.
- 457 [8] V. Sufiiarov, A. Kantyukov, A. Popovich, A. Sotov, Structure and properties of
458 barium titanate lead-free piezoceramic manufactured by binder jetting process,
459 *Materials (Basel).* 14 (2021) 4419. <https://doi.org/10.3390/ma14164419>.
- 460 [9] L.A. Chavez, P. Ibanez, B. Wilburn, D. Alexander, C. Stewart, R. Wicker, Y. Lin, The

- 461 Influence of Printing Parameters, Post-Processing, and Testing Conditions on the
462 Properties of Binder Jetting Additive Manufactured Functional Ceramics, *Ceramics*.
463 3 (2020) 65–77. <https://doi.org/10.3390/ceramics3010008>.
- 464 [10] S.M. Gaytan, M.A. Cadena, H. Karim, D. Delfin, Y. Lin, D. Espalin, E. MacDonald,
465 R.B. Wicker, Fabrication of barium titanate by binder jetting additive manufacturing
466 technology, *Ceram. Int.* 41 (2015) 6610–6619.
467 <https://doi.org/10.1016/j.ceramint.2015.01.108>.
- 468 [11] A. Mostafaei, P. Rodriguez De Vecchis, I. Nettleship, M. Chmielus, Effect of powder
469 size distribution on densification and microstructural evolution of binder-jet 3D-
470 printed alloy 625, *Mater. Des.* 162 (2019) 375–383.
471 <https://doi.org/10.1016/j.matdes.2018.11.051>.
- 472 [12] S. Diener, A. Zocca, J. Günster, Literature Review: Methods for achieving high
473 powder bed densities in ceramic powder bed based additive manufacturing, *Open*
474 *Ceram.* 8 (2021) 100191. <https://doi.org/10.1016/j.oceram.2021.100191>.
- 475 [13] M. Mariani, R. Beltrami, P. Brusa, C. Galassi, R. Ardito, N. Lecis, 3D printing of fine
476 alumina powders by binder jetting, *J. Eur. Ceram. Soc.* 41 (2021) 5307–5315.
477 <https://doi.org/10.1016/j.jeurceramsoc.2021.04.006>.
- 478 [14] R. Beltrami, E. Mercadelli, C. Baldisserri, C. Galassi, F. Braghin, N. Lecis, Synthesis
479 of KNN powders: Scaling effect of the milling step, *Powder Technol.* 375 (2020) 101–
480 108. <https://doi.org/10.1016/j.powtec.2020.07.098>.
- 481 [15] M. Mariani, R. Beltrami, F. Meneghetti, D. Azzolini, N. Lecis, Effect of printing
482 parameters on the mechanical strength of green body from binder jetting additive

- 483 manufacturing, in: *Procedia Eur. 2020 Int. Powder Met. Virtual Congr. Exhib., EPMA,*
484 2020.
- 485 [16] B. Orayech, A. Faik, G.A. López, O. Fabelo, J.M. Igartua, Mode-crystallography
486 analysis of the crystal structures and the low-and high-temperature phase transitions
487 in $\text{Na}_{0.5}\text{K}_{0.5}\text{NbO}_3$, *J. Appl. Crystallogr.* 48 (2015) 318–333.
488 <https://doi.org/10.1107/S1600576715000941>.
- 489 [17] R.M. German, Prediction of sintered density for bimodal powder mixtures, *Metall.*
490 *Trans. A.* 23 (1992) 1455–1465. <https://doi.org/10.1007/BF02647329>.
- 491 [18] W. Du, X. Ren, Y. Chen, C. Ma, M. Radovic, Z. Pei, Model guided mixing of ceramic
492 powders with graded particle sizes in binder jetting additive manufacturing, *ASME*
493 2018 13th Int. Manuf. Sci. Eng. Conf. MSEC 2018. 1 (2018) 1–9.
494 <https://doi.org/10.1115/MSEC2018-6651>.
- 495 [19] Y. Bai, G. Wagner, C.B. Williams, Effect of Particle Size Distribution on Powder
496 Packing and Sintering in Binder Jetting Additive Manufacturing of Metals, *J. Manuf.*
497 *Sci. Eng.* 139 (2017). <https://doi.org/10.1115/1.4036640>.
- 498 [20] M. Moghadasi, W. Du, M. Li, Z. Pei, C. Ma, Ceramic binder jetting additive
499 manufacturing: Effects of particle size on feedstock powder and final part properties,
500 *Ceram. Int.* 46 (2020) 16966–16972. <https://doi.org/10.1016/j.ceramint.2020.03.280>.
- 501 [21] A. Santomaso, P. Lazzaro, P. Canu, Powder flowability and density ratios: The impact
502 of granules packing, *Chem. Eng. Sci.* 58 (2003) 2857–2874.
503 [https://doi.org/10.1016/S0009-2509\(03\)00137-4](https://doi.org/10.1016/S0009-2509(03)00137-4).
- 504 [22] R.B. Shah, M.A. Tawakkul, M.A. Khan, Comparative evaluation of flow for

- 505 pharmaceutical powders and granules, *AAPS PharmSciTech.* 9 (2008) 250–258.
506 <https://doi.org/10.1208/s12249-008-9046-8>.
- 507 [23] Q. Li, V. Rudolph, B. Weigl, A. Earl, Interparticle van der Waals force in powder
508 flowability and compactibility, *Int. J. Pharm.* 280 (2004) 77–93.
509 <https://doi.org/10.1016/j.ijpharm.2004.05.001>.
- 510 [24] Y. Shiratori, A. Magrez, C. Pithan, Particle size effect on the crystal structure
511 symmetry of $K_{0.5}Na_{0.5}NbO_3$, *J. Eur. Ceram. Soc.* 25 (2005) 2075–2079.
512 <https://doi.org/10.1016/j.jeurceramsoc.2005.03.012>.
- 513 [25] T. Do, P. Kwon, C.S. Shin, Process development toward full-density stainless steel
514 parts with binder jetting printing, *Int. J. Mach. Tools Manuf.* 121 (2017) 50–60.
515 <https://doi.org/10.1016/j.ijmachtools.2017.04.006>.
- 516 [26] N. Lecis, M. Mariani, R. Beltrami, L. Emanuelli, R. Casati, M. Vedani, A. Molinari,
517 Effects of process parameters, debinding and sintering on the microstructure of 316L
518 stainless steel produced by binder jetting, *Mater. Sci. Eng. A.* 828 (2021) 142108.
519 <https://doi.org/10.1016/j.msea.2021.142108>.
- 520 [27] Y. Mao, J. Li, W. Li, D. Cai, Q. Wei, Binder jetting additive manufacturing of 316L
521 stainless-steel green parts with high strength and low binder content: Binder
522 preparation and process optimization, *J. Mater. Process. Technol.* 291 (2021) 117020.
523 <https://doi.org/10.1016/j.jmatprotec.2020.117020>.
- 524 [28] B. Malič, J. Koruza, J. Hreščak, J. Bernard, K. Wang, J.G. Fisher, A. Benčan, Sintering
525 of lead-free piezoelectric sodium potassium niobate ceramics, *Materials (Basel)*. 8
526 (2015) 8117–8146. <https://doi.org/10.3390/ma8125449>.

- 527 [29] H.C. Thong, C. Zhao, Z. Zhou, C.F. Wu, Y.X. Liu, Z.Z. Du, J.F. Li, W. Gong, K.
528 Wang, Technology transfer of lead-free (K, Na)NbO₃-based piezoelectric ceramics,
529 *Mater. Today*. 29 (2019) 37–48. <https://doi.org/10.1016/j.mattod.2019.04.016>.
- 530 [30] M. Mariani, I. Goncharov, D. Mariani, G. Pietro De Gaudenzi, A. Popovich, N. Lecis,
531 M. Vedani, Mechanical and microstructural characterization of WC-Co consolidated
532 by binder jetting additive manufacturing, *Int. J. Refract. Met. Hard Mater.* 100 (2021)
533 105639. <https://doi.org/10.1016/j.ijrmhm.2021.105639>.
- 534 [31] D. Huber, L. Vogel, A. Fischer, The Effects of Sintering Temperature and Hold Time
535 on Densification, Mechanical Properties and Microstructural Characteristics of Binder
536 Jet 3D Printed 17-4 PH Stainless Steel, *Addit. Manuf.* 46 (2021) 102114.
537 <https://doi.org/10.1016/j.addma.2021.102114>.
- 538 [32] H. Miyajima, K.M. Rahman, M. Da, C.B. Williams, Effect of fine powder particles on
539 quality of binder jetting parts, *Addit. Manuf.* 36 (2020) 101587.
540 <https://doi.org/10.1016/j.addma.2020.101587>.
- 541 [33] P. Dixit, S. Seth, B. Rawal, B.P. Kumar, H.S. Panda, Freeze casting of lamellar-
542 structured porous lead-free (Na_{0.52}K_{0.48})(Nb_{0.95}Sb_{0.05})O₃ piezoceramic with
543 remarkable enhancement in piezoelectric voltage constant and hydrostatic figure of
544 merit, *J. Mater. Sci. Mater. Electron.* (2021) 1–11. [https://doi.org/10.1007/s10854-](https://doi.org/10.1007/s10854-021-05262-5)
545 [021-05262-5](https://doi.org/10.1007/s10854-021-05262-5).
- 546 [34] J.I. Roscow, H. Pearce, H. Khanbareh, S. Kar-Narayan, C.R. Bowen, Modified energy
547 harvesting figures of merit for stress- and strain-driven piezoelectric systems, *Eur.*
548 *Phys. J. Spec. Top.* 228 (2019) 1537–1554. <https://doi.org/10.1140/epjst/e2019->

549 800143-7.

550 [35] L.A. Chavez, B.R. Wilburn, P. Ibañez, L.C. Delfin, S. Vargas, H. Diaz, C. Fulgentes,
551 A. Renteria, J. Regis, Y. Liu, R.B. Wicker, Y. Lin, Fabrication and characterization of
552 3D printing induced orthotropic functional ceramics, *Smart Mater. Struct.* 28 (2019)
553 125007. <https://doi.org/10.1088/1361-665x/ab4e0a>.

554 [36] J. Roscow, Y. Zhang, J. Taylor, C.R. Bowen, Porous ferroelectrics for energy
555 harvesting applications, *Eur. Phys. J. Spec. Top.* 224 (2015) 2949–2966.
556 <https://doi.org/10.1140/epjst/e2015-02600-y>.

557 [37] Y. Zhang, M. Xie, J. Roscow, Y. Bao, K. Zhou, D. Zhang, C.R. Bowen, Enhanced
558 pyroelectric and piezoelectric properties of PZT with aligned porosity for energy
559 harvesting applications, *J. Mater. Chem. A.* 5 (2017) 6569–6580.
560 <https://doi.org/10.1039/c7ta00967d>.

561 [38] D.J. Shin, D.H. Lim, B.K. Koo, M.S. Kim, I.S. Kim, S.J. Jeong, Porous sandwich
562 structures based on BaZrTiO₃–BaCaTiO₃ ceramics for piezoelectric energy
563 harvesting, *J. Alloys Compd.* 831 (2020).
564 <https://doi.org/10.1016/j.jallcom.2020.154792>.

565